

Accepted by the Astrophysical Journal, 24 Sept. 2004

Joint VLBA/VLTI Observations of the Mira Variable S Orionis

David A. Boboltz

*U.S. Naval Observatory,
3450 Massachusetts Ave., NW, Washington, DC 20392-5420, USA
dboboltz@usno.navy.mil*

and

Markus Wittkowski

*European Southern Observatory,
Karl Schwarzschild-Str. 2, D-85748 Garching bei München, Germany
mwittkow@eso.org*

ABSTRACT

We present the first coordinated VLBA/VLTI measurements of the stellar diameter and circumstellar atmosphere of a Mira variable star. Observations of the $v = 1, J = 1 - 0$ (43.1 GHz) and $v = 2, J = 1 - 0$ (42.8 GHz) SiO maser emission toward the Mira variable S Ori were conducted using the VLBA. Coordinated near-infrared K -band measurements of the stellar diameter were performed using VLTI/VINCI closely spaced in time to the VLBA observations. Analysis of the SiO maser data recorded at a visual variability phase 0.73 show the average distance of the masers from the center of the distribution to be 9.4 mas for the $v = 1$ masers and 8.8 mas for the $v = 2$ masers. The velocity structure of the SiO masers appears to be random with no significant indication of global expansion/infall or rotation. The determined near-infrared, K -band, uniform disk (UD) diameters decreased from ~ 10.5 mas at phase 0.80 to ~ 10.2 mas at phase 0.95. For the epoch of our VLBA measurements, an extrapolated UD diameter of $\Theta_{\text{UD}}^K = 10.8 \pm 0.3$ mas was obtained, corresponding to a linear radius of $R_{\text{UD}}^K = 2.3 \pm 0.5$ AU or $R_{\text{UD}}^K = 490 \pm 115 R_{\odot}$. Our coordinated VLBA/VLTI measurements show that the masers lie relatively close to the stellar photosphere at a distance of ~ 2 photospheric radii, consistent with model estimates. This result is virtually free of the usual uncertainty inherent in comparing observations of variable stars widely separated in time and stellar phase.

Subject headings: masers — stars: AGB and post AGB — stars: atmospheres — stars: late type — stars: mass-loss — techniques: interferometric

1. INTRODUCTION

The evolution of cool luminous stars, including Mira variables, is accompanied by significant mass loss to the circumstellar envelope (CSE) with mass-loss rates of up to $10^{-4} M_{\odot}/\text{year}$ (e.g. Jura & Kleinmann 1990). There are currently a number of tools that can be used to study the stellar surface and the CSE at various wavelengths. Optical/near-infrared long-baseline interferometry has provided information regarding the stellar diameter, effective temperature, center-to-limb intensity variation, and the dependence of these parameters on wavelength and variability phase for a number of Mira variables (e.g., Haniff, Scholz & Tuthill 1995; van Belle et al. 1996; Perrin et al. 1999; Young et al. 2000; Thompson, Creech-Eakman & Akeson 2002a; Thompson, Creech-Eakman & van Belle 2002b; Woodruff et al. 2004). The structure and dynamics of the CSE of Mira variables and supergiants have been investigated by mapping the SiO maser emission at typical distances of 2–4 stellar radii toward these stars using very long baseline interferometry (VLBI) at radio wavelengths (e.g., Boboltz, Diamond & Kemball 1997; Kemball & Diamond 1997; Boboltz & Marvel 2000; Hollis et al. 2001; Diamond & Kemball 2003). Dust shells outward of the SiO maser emission zone have been studied using mid-infrared interferometry (e.g., Danchi et al. 1994; Greenhill et al. 1995; Townes 2003). Near- and mid-infrared interferometry have also been used to study the warm extended atmosphere of Mira variables containing gaseous H₂O, SiO and CO molecules (e.g., Perrin et al. 1999; Mennesson et al. 2002; Ohnaka et al. 2004).

Theoretical models describe and predict photospheric center-to-limb intensity variations including the effect of close molecular layers (e.g., Bessel, Scholz & Wood 1996; Hofmann, Scholz & Wood 1998; Tej et al. 2003; Ireland, Scholz & Wood 2004), the location and dynamics of SiO maser emission zones (Humphreys et al. 1996, 2002), as well as gas and dust components of the stellar winds (e.g., Winters et al. 2000; Hoefner et al. 2003).

Multi-wavelength studies of the stellar surface and the CSE, utilizing a combination of the above techniques, are well suited to study the structure of the CSE, the mass-loss process, and the evolution of these stars. It is common for infrared observations of the stellar photosphere or the circumstellar dust to be compared to radio observations of circumstellar masers from the literature and vice versa. For example, Danchi et al. (1994) compared the inner radii and extents of dust shells as determined from Infrared Spatial Interferometer (ISI) observations with estimates of the photospheric radii and measurements of the extents of the SiO, H₂O, and OH maser shells. Similarly, Monnier et al. (2004) compared high-resolution data on the stellar diameters and dust shells of two stars (VX Sgr and NML Cyg) from Keck aperture masking and Infrared Optical Telescope Array (IOTA) interferometry with previously published maps of the SiO maser emission toward these stars. Such comparisons, however, are somewhat limited due to the inherent variability in the CSE and the star itself. The SiO masers for example have been shown to have proper motions and intensity variations on time scales of a few weeks (Boboltz, Diamond & Kemball 1997; Diamond & Kemball 2003). Similarly, interferometric measurements of the stellar parameters vary with stellar variability phase as discussed above. This inherent variability of Mira stars and their surroundings necessitates a more coordinated approach to multi-wavelength studies of these objects.

The first such coordinated multi-wavelength study of a late-type variable was performed by Greenhill et al. (1995) for the star VX Sgr. Coordinated measurements included both mid-infrared observations to determine the extent of the circumstellar dust shell and VLBI mapping of the SiO maser zone. More recently, Cotton et al. (2004) compared Very Long Baseline Array (VLBA) images of the SiO maser emission of several Mira stars with near-infrared diameters obtained at the Infrared Optical Telescope Array (IOTA) interferometer (Mennesson et al. 2002), and with literature values of the mid-infrared dust shell extensions.

Here, we present the first results from a series of coordinated VLTI/VLBA observations of late-type variable stars, in particular, for the Mira variable S Ori. Our results include the first radio interferometric images of the SiO masers (VLBA) and the most accurate photospheric diameter measurements using near-infrared K -band interferometry (VLTI/VINCI).

2. CHARACTERISTICS OF S ORI

The target of our observations, S Ori, is a Mira variable star with spectral type M6.5-M9.5e (Kholopov et al. 1985) and V magnitude 8.4-13.3 (Pojmanski 2002). Whitelock, Marang & Feast (2000) report a quite low near-infrared J -band pulsation amplitude of 0.55 mag. They also derive a mean bolometric magnitude $m_{\text{bol}} = 3.08$, with an amplitude $\Delta m_{\text{bol}} = 0.49$. Over the last 100 years, the variability period of S Ori has been seen to randomly vary between about 400 and 450 days (Bedding et al. 1999; Whitelock, Marang & Feast 2000; Merchán Benítez & Jurado Vargas 2002). For our study, we adopt a stellar period of 420 days and a time of last maximum visual brightness of JD 2452331, as given by Pojmanski (2002). This is consistent within $\pm \sim 5$ days with an inspection of the most recent AAVSO and AFOEV data. van Belle et al. (1996) measured the near-infrared K -band uniform disk (UD) diameter of S Ori at variability phase 0.56 to be 10.54 ± 0.68 mas, and derived a Rosseland mean diameter of 11.70 ± 0.75 mas. We adopt the distance to S Ori to be 422 ± 37 pc, as given by van Belle et al. (1996), based on measurements by Wyatt & Cahn (1983) and Young (1995). This is consistent with the value of 430 pc from Whitelock, Marang & Feast (2000) based on their K period-luminosity relation. S Ori exhibits SiO and OH masers (Benson et al. 1990), but no detection of any H₂O maser emission has been reported. Sloan & Price (1998) report a relatively low dust emission coefficient (DEC), i.e. the total emission of the dust to the total emission of the star in the wavelength range from 7.7–14.0 μm , of 0.24 for S Ori (for comparison, $DEC = 0.46$ for α Cet).

3. OBSERVATIONS AND REDUCTION

3.1. Near-infrared K -band interferometry

We obtained near-infrared K -band interferometric measurements of S Ori using the ESO Very Large Telescope Interferometer (VLTI) equipped with the commissioning instrument VINCI and the two VLTI test siderostats (effective apertures ~ 40 cm). VLTI stations D 1 and B 3, forming an unprojected baseline length of 24 m, were used for 13 nights between 2003 January 25 (JD 2452665) and 2003 March 31 (JD 2452730). The S Ori visual variability phase ranged from 0.80 to 0.95 for these dates. Available data taken in 2002 December using an 8 m ground baseline and in 2003 September using a 16 m ground baseline were not used because S Ori was only marginally resolved with these shorter baselines ($|V| \gtrsim 0.9$). A recent general description of the VLTI can be found in Glindemann et al. (2003) and references therein. During each observation night, several series of typically 500 interferogram scans were recorded on S Ori as well as on several calibration stars. The calibration stars used and their adopted properties are listed in Table 1. For S Ori, an effective temperature of 2500 K was used, which is consistent with the value of 2313 ± 110 K obtained by van Belle et al. (1996) for phase 0.56. We note that variations of the effective temperatures up to ± 500 K result in variations of the squared visibility amplitude of less than 0.3%. The scan length for the S Ori and all calibration stars' observations was $230 \mu\text{m}$, the scan speed was $616 \mu\text{m/sec}$, and the fringe frequency, corresponding to the time to scan one interferometric fringe, was 289.5 Hz.

Mean coherence factors were obtained for each series of interferograms using the VINCI data reduction software, version 3.0, as described by Kervella et al. (2004), employing the results based on wavelets transforms. Calibrated squared visibility values for S Ori were obtained by calibration of the mean coherence factors as described in Wittkowski et al. (2004), with a time kernel of 5 hours to convolve the measured transfer function. The errors of the calibrated S Ori squared visibility values include the scatter of the single-scan coherence factors, the adopted errors of the diameters of the calibration stars, and the observed variation of the transfer function during each night. The calibrated visibility values are listed in Table 2 and are also available in electronic form from the authors upon request. Table 2 also lists the date and time of observation, the spatial frequency, the position angle of the projected baseline (East of North), the calibrated squared visibility value V^2 and its error σ_{V^2} , as well as the number of processed interferograms. The effective wavelength is $2.19 \mu\text{m}$. All observations were performed at similar angles of the projected baseline ranging from $72^\circ - 74^\circ$ E of N. The squared visibility values for S Ori were grouped into four bins of five nights each (bin width $\sim 1\%$ of the visual variability period of 420 days).

We characterize our measurements with a best-fitting uniform disk (UD) diameter for each of our four epochs. Our uniform disk model takes into account the broad passband ($1.9 - 2.5 \mu\text{m}$) of the VINCI instrument, as described in Wittkowski et al. (2004). Figure 1 shows the obtained squared visibility amplitudes of S Ori together with the best fitting uniform disk models for each of our four VLTI/VINCI epochs. The larger scatter of the visibility data for the March 16-21 epoch, as compared to the other epochs, can be explained by a larger time difference of the calibration stars.

Table 3 lists the observation dates and the determined K -band UD diameters and their associated formal errors. Additional calibration uncertainties are estimated to be ~ 0.1 mas, based on an analysis of sub-volumes of the data and differing methods of interpolating the transfer function. The addition of a possible circumstellar dust shell is not expected to affect the K -band UD diameter significantly (see for instance discussions in Woodruff et al. 2004; Ohnaka et al. 2004). In particular, Ohnaka et al. (2004) modeled an optically thin dust disk for a similar Mira star, RR Sco (dust emission coefficient 0.21, compared to the value of 0.24 for S Ori), for the purpose of comparison to mid-infrared interferometric data. At a wavelength of $2.2\ \mu\text{m}$ the scattered and thermal emission from this dust disk is lower by a factor of ~ 1000 compared to the attenuated star light and the effect on the squared visibility values at $V^2 \sim 0.5$ is less than 0.2% (Ohnaka, K. 2004, private communication). This would lead to an effect on the uniform disk diameters in Tab. 3 of less than 0.02 mas. Discussed in Sect. 4.1 below is the relationship between a K -band UD diameter and a physically more meaningful angular size of the stellar photosphere.

3.2. SiO Maser Observations

We simultaneously observed the $v = 1, J = 1 - 0$ (43.1 GHz) and $v = 2, J = 1 - 0$ (42.8 GHz) SiO maser transitions toward S Ori ($\alpha = 05^h29^m00^s.9, \delta = -04^\circ41'32''.7$, J2000) on 2002 December 29 for 6 hrs starting at 02:43 UT (JD 2452636.6, visual variability phase 0.73). S Ori and a continuum calibrator (0359+509) were observed using the 10 stations of the VLBA. The VLBA is operated by the National Radio Astronomy Observatory (NRAO).¹ Reference frequencies of 43.122080 and 42.820587 GHz were used for the $v = 1$ and $v = 2$ SiO transitions respectively. Data were recorded in dual circular polarization using two 8-MHz ($56.1\ \text{km s}^{-1}$) bands centered on the local standard of rest (LSR) velocity of $18.0\ \text{km s}^{-1}$. System temperatures and point source sensitivities were on the order of ~ 150 K and $\sim 11\ \text{Jy K}^{-1}$ respectively.

The data were correlated at the VLBA correlator operated by NRAO in Socorro, New Mexico. Auto and cross-correlation spectra consisting of 256 channels with channel spacings of 31.25 kHz ($\sim 0.2\ \text{km s}^{-1}$) were produced by the correlator. Calibration was performed using the Astronomical Image Processing System (AIPS) maintained by NRAO. The total intensity data were calibrated in accordance with the procedures outlined in Diamond (1989). The bandpass response was determined from scans on the continuum calibrator and used to correct the target source data. The time-dependent gains of all antennas relative to a reference antenna were determined by fitting a total-power spectrum (from the reference antenna with the target source at a high elevation) to the total power spectrum of each antenna. The absolute flux density scale was established by scaling these gains by the system temperature and gain of the reference antenna. Errors in the gain and pointing of the reference antenna and the atmospheric opacity contribute to the error in the

¹The National Radio Astronomy Observatory is a facility of the National Science Foundation operated under cooperative agreement by Associated Universities, Inc.

absolute amplitude calibration, which is accurate to about 15–20%.

To correct any instrumental delay, a fringe fit was performed on the continuum calibrator scans, and residual group delays for each antenna were determined. Variations in the residual delays ranged from 2–4 ns resulting in phase errors of no more than 1.5–3° across the 8-MHz band. Residual fringe-rates were obtained by fringe-fitting a strong reference feature in the spectrum of each maser transition. For both transitions we used the same channel at a velocity $V_{\text{LSR}} = 16.2 \text{ km s}^{-1}$. The resulting fringe-rate solutions were applied to all channels in each spectrum respectively. An iterative self-calibration and imaging procedure was then performed to map this reference channel for each transition. The resulting residual phase and amplitude corrections from the reference channels at 42.8 and 43.1 GHz were applied to all channels in the respective bands.

In order to accurately compare the distributions of the two maser transitions, it is desirable to determine a common spatial reference point. However, after the fringe-fitting step to determine residual fringe-rates, all absolute position information is lost for the VLBA data. We accomplished the registration of the two transitions by applying the fringe-fit solutions from the $v = 2$, 42.8-GHz transition to the $v = 1$, 43.1-GHz data, re-mapping the $v = 1$ transition, and comparing the resulting images with those produced from the application of the $v = 1$ calibration itself. Although the images resulting from the application of the 42.8-GHz fringe-fit to the 43.1-GHz data were of poorer quality, we were still able to determine an offset between the two sets of images. The offsets in right ascension and declination computed from images of two different spectral channels, were the same to within 0.03 mas. Subsequent phase self-calibration and imaging were performed for the $v = 1$ SiO data using these computed offsets, resulting in spatially aligned $v = 1$ and $v = 2$ image cubes. This same procedure was applied to the continuum calibrator source, 0359+509, and the positions derived agreed to within 0.4 mas, thus providing an estimate of the error in the registration of the two maser distributions.

Final images of the SiO maser emission consisting of 1024×1024 pixels ($\sim 51 \times 51$ mas) were generated using synthesized beams of 0.58×0.17 mas and 0.52×0.17 mas for the $v = 1$ and $v = 2$ transitions respectively. Images were produced for spectral channels from 4.7 km s^{-1} to 30.7 km s^{-1} forming image cubes of 120 planes. Off-source RMS noise in the images ranged from 7 mJy to 18 mJy. Figure 2 shows the total intensity contour maps of the $v = 1$, 43.1-GHz (red) and $v = 2$, 42.8-GHz (blue) SiO maser emission toward S Ori. The contours represent the maximum pixel value in each image cube over the LSR velocity range from $+10.1 \text{ km s}^{-1}$ to $+25.4 \text{ km s}^{-1}$. Subsequent analysis of the image data is described in detail in Sect. 4.2.

4. RESULTS AND DISCUSSION

4.1. The photospheric diameter

Figure 3 and Tab. 3 show our near-infrared K -band uniform disk (UD) diameters of S Ori determined from our four VLTI/VINCI epochs as a function of observation date and visual variability phase, as discussed in Sect. 3.1. The K -band UD diameter decreases almost linearly from ~ 10.5 mas at visual variability phase 0.80 to ~ 10.2 mas at phase 0.95, i.e. by $\sim 3\%$. It is not clear whether the local diameter minimum of ~ 10.0 mas at phase 0.92 in Tab. 3 and Fig. 3 is caused by an additional systematic calibration error as discussed in Sect. 3.1, or by a real minimum of the stellar size. The minimum of a Mira K -band UD diameter is predicted to lie at visual variability phase ~ 0.9 , according to model predictions by Ireland, Scholz & Wood (2004). Our coordinated VLBA measurement at visual variability phase 0.73 occurred about one month before the first VLTI epoch at phase 0.8, and is hence close to, but not exactly contemporaneous to the VLTI epochs. Both, observations of the diameter change of the Mira star S Lac by Thompson, Creech-Eakman & van Belle (2002b) as well as Mira star model predictions by Ireland, Scholz & Wood (2004) show an almost linear change of the K -band UD diameter between variability phases 0.7 and 0.9, i.e. in the pre-minimum part of the diameter curve and pre-maximum part of the visual light curve. Thus, we can linearly extrapolate our K -band UD diameter data at phases 0.8–0.95 to the VLBA phase 0.73. For phase 0.73, we determine an extrapolated K -band UD diameter of $\Theta_{\text{UD}}^K(\text{VLBA epoch, phase} = 0.73) = 10.8 \pm 0.3$ mas. This value and its error correspond to the mean and difference of the two linear extrapolations shown in Fig. 3, which used all four points and only the two closest points to the VLBA epoch respectively. This UD diameter corresponds to a linear radius $R_{\text{UD}}^K = 2.3 \pm 0.5$ AU or $R_{\text{UD}}^K = 490 \pm 115 R_{\odot}$ with our assumed distance to S Ori.

A UD intensity profile is often not an ideal representation of the true near-infrared center-to-limb intensity variation (CLV) of cool giants in general and of Mira stars in particular. The CLV of cool giants has been studied by, e.g. Quirrenbach et al. (1996); Burns et al. (1997); Scholz (1998); Hofmann, Scholz & Wood (1998); Wittkowski et al. (2001, 2004); Ireland, Scholz & Wood (2004); Woodruff et al. (2004). UD diameters of non-variable giants obtained from visibility measurements in the first lobe are usually transformed into physically more meaningful Rosseland angular diameters using correction factors determined from atmosphere models in the literature (e.g. Claret 2003). For the case of Mira variable stars, few atmosphere models are available. We used the hydrodynamic atmosphere models from Hofmann, Scholz & Wood (1998); Tej et al. (2003); Ireland, Scholz & Wood (2004), to estimate the relationship between the K -band UD diameter and the continuum diameter. While the broad-band UD diameter is affected by various molecular bands, the continuum diameter is a better estimate of the real photospheric stellar size. These models have been constructed for the prototype Mira stars α Cet and R Leo and have been compared to observations of several Mira stars by, for instance, Hofmann et al. (2001, 2002); Woodruff et al. (2004). The general model results are not expected to be dramatically different for other Mira stars such as S Ori (Scholz, M. 2004, private communication). The model predicted

difference between the continuum and K -band UD diameters is relatively low in the pre-maximum region of the visual variability curve as in the case of our observations. At this phase of 0.73, the continuum diameter may be smaller than the K -band UD diameter by about 15% (Ireland, Scholz & Wood 2004). With this assumption, the continuum photospheric diameter for the epoch of our VLBA observation would be $\Theta_{\text{Phot}}(\text{VLBA epoch, phase} = 0.73) \approx 9.2 \text{ mas}$. This angular radius corresponds to a photospheric radius of $R_{\text{Phot}} \approx 420 R_{\odot}$ or $R_{\text{Phot}} \approx 1.9 \text{ AU}$ with our assumed distance to S Ori. With a bolometric flux of $m_{\text{bol}} = 3.1 \pm 0.3$ (Whitelock, Marang & Feast 2000), our value for Θ_{Phot} corresponds to an effective temperature $T_{\text{eff}} \approx 2670 \text{ K}$.

4.2. The $v = 1$ and $v = 2$ SiO Maser Emission

Our total intensity images of the 43.1 GHz and 42.8 GHz SiO maser emission (Figure 2) show a typical clumpy distribution of the maser spots within a ring-like structure. For the $v = 2$, 42.8-GHz transition the ring is relatively sparse with nearly all of the masers concentrated to the NW side of the shell, and a few features to the SE. The $v = 1$, 43.1-GHz masers, however, form a more typical ring-like structure often seen for other stars with SiO masers. Like the $v = 2$ masers, the $v = 1$ SiO also has a higher concentration of features on the NW side of the shell. The $v = 1$ maser ring appears to be symmetrical, forming a nearly circular shell. The distribution of the $v = 2$ SiO masers is too sparse to allow us to comment on any symmetry for this transition.

In order to identify and parameterize maser components, two-dimensional Gaussian functions were fit to the emission in each spectral (velocity) channel using the AIPS task SAD. Image quality was assessed using the off-source RMS noise and the deepest negative pixel in the image. A cutoff flux density was conservatively set to the greater of $8\sigma_{\text{RMS}}$ or the absolute value of the deepest negative pixel in the plane. Features with flux densities greater than this cutoff were fit with Gaussians to determine component parameters. Errors in the positions in right ascension and declination of identified features were computed using the fitted source size divided by twice the signal-to-noise ratio (SNR) in the image and ranged from $1 \mu\text{as}$ for features with high SNR, to $50 \mu\text{as}$ for features with lower SNR.

Since the $\sim 0.2 \text{ km s}^{-1}$ channel spacing is sufficient to resolve the masers spectrally, features typically appear in multiple adjacent spectral channels. Positions in right ascension and declination and center velocities for the masers were determined using a flux-density-squared weighted average for features identified in two or more adjacent channels with a spatial coincidence of 0.2 mas ($\sim 2/3$ of the geometric mean of the synthesized beam). The flux assigned to the maser averages was the maximum single-channel flux density. The maser components identified using this procedure are represented by the circles in Figures 4 and 5. In the figures, point sizes are proportional to the logarithm of the fitted flux density which ranged from 0.2 to 4.3 Jy for Figure 4 and 0.1 to 5.3 Jy for Figure 5. The line-of-sight (LOS) velocity information for the masers is also represented in Figures 4 and 5. The top panel of each figure shows the spectrum of SiO maser emission ranging from 10 to 25 km s^{-1} color-coded by LOS velocity in increments of 2 km s^{-1} . The bottom panels of Figures 4

and 5 show the spatial distribution of the SiO masers plotted with the same velocity color-coding as in the top panel, and with the color of the maser representing its corresponding velocity range in the spectrum. Comparing the maser component maps with the total intensity contour maps, we see that the identified features accurately represent the emission summed over all velocity channels in the image cube. From the component maps there does not appear to be any coherent velocity structure indicative of global expansion/infall or rotation. We do note that a group of components on the western side of the shell shows a velocity gradient with velocity decreasing with increasing distance from the star. Such velocity gradients in the SiO maser emission have been observed previously (e.g. Boboltz & Marvel 2000; Hollis et al. 2001).

To compare the size of the SiO maser distribution to the photospheric diameter of the star as measured by the near-infrared K -band interferometry we determined the average distance of the masers from the center of the distribution. To accomplish this, we first determined the center of the distribution by performing a least-squares fit of a circle to the combined $v = 1$ and $v = 2$ maser component data. This fit produced a common center from which we computed the mean maser angular distance \bar{r}_{SiO} and the standard deviation for each transition independently. The mean angular distances from center for the observed SiO masers at $v = 1$, 43.1-GHz and $v = 2$, 42.8-GHz are $\bar{r}_{\text{SiO}} = 9.4$ and $\bar{r}_{\text{SiO}} = 8.8$ mas respectively. These distances are indicated by a dashed circle and are listed in the lower panel of Figures 4 and 5. Standard deviations of the distances are $\sigma_{\text{SiO}} = 1.4$ and $\sigma_{\text{SiO}} = 1.7$ mas for the $v = 1$ and $v = 2$ transitions respectively. The standard deviations provide an indication of the thickness of the shell and are likely dominated by the features on the western side of the shell with a wide range of distances from the center. The mean angular distances we derive are consistent with least-squares circle fits to each distribution independently using the previously mentioned common center. The least-squares fits to each transition have the added assumption that the distribution is circular, thus we have chosen to report only the mean distance from center. The computed angular distances translate to linear shell distances from center of 4.0 ± 0.6 AU and 3.7 ± 0.6 AU at the assumed distance of 422 ± 37 pc. The standard deviations are likewise 0.6 ± 0.1 AU and 0.7 ± 0.1 AU for the $v = 1$ and $v = 2$ masers respectively.

In principal, a comparison of the relative spatial locations of the $v = 1$ and $v = 2$ masers should allow us to comment on possible pumping mechanisms (i.e. collisional, radiative, or combination) as in Desmurs et al. (2000). However, because the $v = 2$, 42.8-GHz masers are mostly confined to a small region on the NW side of the shell, it is difficult to unambiguously determine the relative shift between the two maser shells. Although the mean distance from center we determine for the $v = 2$ masers is slightly smaller than the $v = 1$ mean distance, the two values are consistent to within the errors.

4.3. Comparison of SiO maser distribution and photospheric stellar diameter

Figures 4 and 5 also provide a comparison of the distribution of the SiO maser spots with our obtained angular size of the photospheric disk at the same epoch. The average distance of the maser

spots from the center of their distribution for the 43.1 GHz and 42.8 GHz transitions ($\bar{r}_{\text{SiO}} = 9.4$ mas and $\bar{r}_{\text{SiO}} = 8.8$ mas) appears at $1.7 R_{\star}$ and $1.6 R_{\star}$ respectively when compared to our estimate of the K -band UD diameter. When compared to our estimate of the continuum diameter these values are slightly larger at $2.0 R_{\star}$ and $1.9 R_{\star}$ respectively. The widths of the distributions are approximately $0.3 R_{\star}$ for the masers in both transitions. As a reference the angular photospheric radius is listed in the lower panel of Figures 4 and 5 and is indicated by a colored circle at the center of the maser distribution. The position of the near-infrared stellar disk as indicated on the plots is assumed to coincide with the center of the SiO maser distribution as discussed in Sect. 4.2. The true location of the star relative to the masers is still unknown. We note that the above estimates are based on angular sizes derived for the SiO maser emission and the near-infrared photosphere, and hence are independent of the distance to S Ori. This result is consistent with theoretical estimates by Humphreys et al. (2002) based on a stellar hydrodynamic pulsation model combined with an SiO maser model. They obtain values between $1.7 R_{\star}$ and $2.1 R_{\star}$, depending on the variability phase.

Our result is consistent with a SiO maser ring radius of approximately $2 R_{\star}$ as determined by Cotton et al. (2004) for several Mira variables. Recently, however, Monnier et al. (2004) updated the stellar diameter estimate of Greenhill et al. (1995) for the supergiant VX Sgr and found that the SiO masers lie at a greater distance from the photosphere, $3.9 R_{\star}$, rather than the $1.3 R_{\star}$ determined by Greenhill et al. (1995). It is striking that the stellar diameter for the other supergiant observed by Monnier et al. (2004), NML Cyg, also indicates a SiO maser ring distance of $\sim 4 R_{\star}$ when compared to the SiO maser shell diameter obtained by Boboltz & Marvel (2000). It is unclear whether these larger distances are an artifact caused by the non-contemporaneous measurements or, whether they indicate an inherent difference between Miras and supergiants. In earlier studies, measured sizes for SiO maser shells have been compared to stellar sizes based on diameters found in the literature (e.g. Boboltz, Diamond & Kemball 1997; Boboltz & Marvel 2000; Hollis et al. 2001). These diameters are often widely spaced in time and stellar phase from the measurements of the SiO maser shell. Sometimes the stellar diameters have not been measured at all and comparisons are made with even less precise diameter estimates based on the luminosity of the star (e.g. Diamond et al. 1994; Colomer et al. 1996; Sánchez Contreras et al. 2002). These examples demonstrate that it is desirable to compare SiO maser ring diameters with stellar diameter estimates, and highlight the need for contemporaneous multi-wavelength observations.

5. SUMMARY

Using the VLBA and VLTI/VINCI, we have undertaken a coordinated multi-wavelength study of the Mira variable S Ori. The VLBA observations resulted in the first interferometric images of the $v = 1, J = 1 - 0$, 43.1-GHz and the $v = 2, J = 1 - 0$, 42.8-GHz SiO transitions. These images show that the masers lie in a clumpy ring-like distribution. Analysis of the VLBA images provided mean distances from center of 9.4 mas (4.0 AU) and 8.8 mas (3.7 AU) and standard deviations of 1.4 mas (0.6 AU) and 1.7 mas (0.7 AU) for the $v = 1$ and $v = 2$ SiO masers respectively at a stellar phase

of 0.73. From near-infrared K -band visibility measurements made with VLTI/VINCI, we derived UD diameters that decreased over time from ~ 10.5 mas at stellar phase 0.80 to ~ 10.2 mas at phase 0.95. After extrapolating the UD diameter to the phase of our VLBA observations and considering a correction from UD diameter to continuum photospheric size, we determine a photospheric diameter of $\Theta_{\text{Phot}} \approx 9.2$ mas, corresponding to a linear radius of $R_{\text{Phot}} \approx 1.9$ AU.

Because these observations of S Ori were closely spaced in time in a coordinated effort between the two instruments, we are able to relate the stellar diameter with the size of the SiO maser shell without the uncertainty caused by the inherent variability of the star. Thus we can conclusively say that the SiO masers lie relatively close to the stellar photosphere at a distance of $\sim 2 R_{\star}$ at the time of our observations.

The observations presented here represent the first in a series of coordinated VLBA/VLTI experiments to study long-period variable stars. The present VLTI observations were obtained during the commissioning period of the VLTI with the commissioning instrument VINCI and the small (40 cm) test siderostats. Future observations will utilize the scientific VLTI instruments in the mid-infrared (MIDI) and near-infrared (AMBER) with the 8 m Unit Telescopes and 1.8 m Auxiliary Telescopes. The upcoming near-infrared VLTI instrument AMBER will allow interferometric measurements in the near-infrared J , H , and K bands with a spectral resolution of up to 10 000, and will provide closure phases. This will enable us to directly measure the the continuum stellar diameter and to study the conditions on the stellar surface, including possible asymmetries and surface inhomogeneities.

The near-infrared results are based on public data collected at the ESO VLTI, Paranal, Chile, in the framework of our P70 shared risk program. We acknowledge support by the ESO DGDF. We are grateful to M. Scholz for valuable comments with respect to definitions of Mira star radii. We thank as well T. Driebe and K. Ohnaka for helpful discussions. MW is grateful for hospitality at the U.S. Naval Observatory. DAB is grateful for the hospitality at the European Southern Observatory.

REFERENCES

Bedding, T. R., Conn, B. C., & Zijlstra A. A. 1999, ASP Conf. Ser., 203, L. Szabados and D. Kurtz (eds.), p. 96, astro-ph/9911070

Benson, P. J., Little-Marenin, I. R., Woods, T. C., Attridge, J. M., Blais, K. A., Rudolph, D. B., Rubiera, M. E., Keefe, H. L. 1990, ApJS, 74, 911

Bessel, M. S., Scholz, M., & Wood, P. R. 1996, A&A, 307, 481

Boboltz, D. A., Diamond, P.J., & Kemball, A.J. 1997, ApJ, 487, L147

Boboltz, D. A., & Marvel, K. B. 2000, ApJ, 545, L149

Bordé, P. J., Coudé du Foresto, V., Chagnon, G., & Perrin, G. 2002, A&A393, 183

Burns, D., et al. 1997, MNRAS, 290, L11

Claret, A. 2003, A&A, 401, 657

Colomer, F., Baudry, A., Graham, D. A., Booth, R. S., de Vicente, P., Krichbaum, T. P., Gomez-Gonzalez, J., & Schalinski, C. 1996, A&A, 312, 950

Cotton, W. D., et al. 2004, A&A, 414, 275

Danchi, W. C., Bester, M., Degiacomi, C. G., Greenhill, L. J., & Townes, C. H. 1994, AJ, 107, 1469

Desmurs, J.-F., Bujarrabal, V., Colomer, F., & Alcolea, J. 2000, A&A, 360, 189

Diamond, P. J. 1989, in Very Long Baseline Interferometry: Techniques and Applications, eds. M. Felli & R.E. Spencer, (Dordrecht: Kluwer Academic Press), 233

Diamond, P. J., Kemball, A. J., Junor, W., Zensus, A., Benson, J., & Dhawan, V. 1994, ApJ, 430, L61

Diamond, P. J., & Kemball, A. J. 2003, ApJ, 599, 1372

Glindemann, A., et al. 2003, Proc. SPIE, 4838, 89

Greenhill, L. J., Colomer, F., Moran, J. M., Backer, D. C., Danchi, W. C., & Bester, M. 1995, ApJ449, 365

Haniff, C. A., Scholz, M., & Tuthill, P. G. 1995, MNRAS, 276, 640

Hoefner, S., Gautschy-Loidl, R., Aringer, B., & Jorgensen, U. G., 2003, A&A399, 589

Hofmann, K.-H., et al. 2002, New Astronomy, 7, 9

Hofmann, K.-H., Balega, Y., Scholz, M., & Weigelt, G. 2001, A&A, 376, 518

Hofmann, K.-H., Scholz, M., & Wood, P. R. 1998, A&A, 339, 846

Hollis, J. M., Boboltz, D. A., Pedelty, J. A., White, S. M., & Forster, J. R. 2001, ApJ, 559, L37

Humphreys, E. M. L., Gray, M. D., Yates, J. A., Field, D., Bowen, G., & Diamond, P. J. 1996, MNRAS, 282, 1359

Humphreys, E. M. L., Gray, M. D., Yates, J. A., Field, D., Bowen, G., & Diamond, P. J. 2002, A&A386, 256

Ireland, M. J., Scholz, M., & Wood, P. R. 2004, MNRAS, 352, 318

Jura, M., & Kleinmann, S. G. 1990, ApJS, 73, 769

Kemball, A. J., & Diamond, P. J. 1997, ApJ, 481, L111

Kervella, P., Ségransan, D., & Coudé du Foresto, V., 2004, A&A, in press

Kholopov, P. N., et al. 1985, General Catalogue of Variable Stars 4th ed. (GCVS4), Moscow: Nauka Publishing House

Mennesson, B. et al. 2002, ApJ, 579, 446

Merchán Benítez, P., & Jurado Vargas, M. 2002, A&A, 386, 244

Monnier, J. D., et al. 2004, ApJ, 605, 436

Ohnaka, K., et al. 2004, A&A, in press

Perrin, G., Coudé du Foresto, F., Ridgway, S. T., Mennesson, B., Ruilier, C., Mariotti, J.-M., Traub, W. A., & Lacasse, M. G. 1999, A&A, 345, 221

Pojmanski, G. 2002, Acta Astronomica, 52, 397

Quirrenbach, A., Mozurkewich, D., Buscher, D. F., Hummel, C. A., & Armstrong, J. T. 1996, A&A, 312, 160

Sánchez Contreras, C., Desmurs, J. F., Bujarrabal, V., Alcolea, J., & Colomer, F. 2002, A&A, 385, L1

Scholz, M. 1998, IAU Symp. 189: Fundamental Stellar Properties, 189, 51

Sloan, G. C. & Price, S. D. 1998, ApJS, 119, 141

Tej, A., Lancon, A., Scholz, M., & Wood P. R., 2003, A&A, 412, 481

Thompson, R. R., Creech-Eakman, M. J., & Akeson, R. 2002, ApJ, 570, 373

Thompson, R. R., Creech-Eakman, M. J., & van Belle, G. T. 2002, *ApJ*, 577, 447

Townes, C. H. 2003, *Rev. of Mod. Astr.*, 16, 1

van Belle, G., Dyck, M., Benson, J., & Lacasse, M. 1996, *AJ*, 112, 2147

Whitelock, P., Marang, F., & Feast, M. 2000, *MNRAS*, 319, 728

Winters, J. M., Le Bertre, T., Jeong, K. S., Helling, C., & Sedlmayer, E. 2000, *A&A*361, 641

Wittkowski, M., Hummel, C. A., Johnston, K. J., Mozurkewich, D., Hajian, A. R., & White N. M. 2001, *A&A*, 377, 981

Wittkowski, M., Aufdenberg J. P., & Kervella, P. 2004, *A&A*, 413, 711

Woodruff, H. C., et al. 2004, *A&A*, 421, 703

Wyatt, J. H., & Cahn, S. P. 1983, *ApJ*, 275, 225

Young, K. 1995, *ApJ*, 445, 872

Young, J. S., et al. 2000, *MNRAS*, 318, 381

Table 1. Properties of the observed VLTI/VINCI calibration stars (Bordé et al. 2002).

Star	Θ_{UD}^K (mas)	$\sigma(\Theta)$ (mas)	T_{eff} (K)
18 Mon	1.86	0.023	4656
31 Ori	3.56	0.057	4046
58 Hya	3.12	0.035	4318
α CMa	5.94	0.016	9900
δ Lep	2.56	0.041	4656
ϵ Lep	5.91	0.064	4046
HD 112213	3.15	0.036	3690
HD 132833	3.06	0.034	3690
HR 2305	1.76	0.031	4256
HR 2311	2.43	0.040	4046
HR 3803	6.93	0.079	4046
ξ^2 Sgr	3.28	0.036	4508
ν^2 CMa	2.38	0.026	4497
τ Sgr	3.83	0.043	4444

Table 2. Calibrated VLTI/VINCI visibility values.

Date	Time	Spat. Freq. (1'')	Basel. Angle (° E of N)	V^2	σ_{V^2}	#
2003-01-26	01:56:48	52.88	72.23	4.447e-01	1.053e-02	479
2003-01-26	02:02:42	52.98	72.38	4.431e-01	1.056e-02	458
2003-01-26	02:09:00	53.05	72.53	4.358e-01	1.062e-02	416
2003-01-26	02:47:04	52.68	73.19	4.465e-01	1.093e-02	453
2003-01-26	02:53:21	52.49	73.26	4.462e-01	1.101e-02	436
2003-01-26	02:59:39	52.26	73.31	4.455e-01	1.106e-02	462
2003-01-26	03:11:06	51.76	73.38	4.689e-01	1.194e-02	432
2003-01-26	03:17:07	51.45	73.40	4.576e-01	1.208e-02	412
2003-01-26	03:23:36	51.08	73.41	4.639e-01	1.495e-02	377
2003-01-26	04:11:15	47.21	73.03	5.237e-01	2.989e-02	256
2003-01-26	04:17:31	46.56	72.92	5.417e-01	3.260e-02	250
2003-01-26	04:36:44	44.37	72.45	5.615e-01	2.009e-02	241
2003-01-26	04:43:26	43.55	72.25	5.695e-01	1.948e-02	210
2003-01-31	02:40:32	52.24	73.32	4.838e-01	4.282e-02	145
2003-01-31	02:51:39	51.75	73.38	4.662e-01	4.361e-03	479
2003-01-31	02:57:52	51.43	73.40	4.753e-01	4.382e-03	485
2003-01-31	03:49:26	47.43	73.07	5.284e-01	7.397e-03	365
2003-02-05	03:53:23	44.86	72.56	5.598e-01	1.807e-02	364
2003-02-05	04:05:16	43.40	72.21	5.980e-01	2.105e-02	232
2003-02-06	03:26:20	47.38	73.06	5.323e-01	1.217e-02	471
2003-02-06	03:58:48	43.72	72.29	5.949e-01	1.483e-02	388
2003-02-10	01:08:45	53.04	72.50	5.110e-01	4.295e-02	159
2003-02-10	01:28:27	53.03	72.91	4.723e-01	2.416e-02	427
2003-02-10	02:17:13	51.50	73.40	4.962e-01	2.543e-02	454
2003-02-10	02:23:25	51.15	73.41	4.950e-01	2.536e-02	456
2003-02-10	02:29:57	50.74	73.41	5.159e-01	2.668e-02	443
2003-02-10	03:24:02	45.96	72.80	5.803e-01	4.593e-02	250
2003-03-17	00:26:00	49.77	73.36	5.115e-01	7.606e-03	323
2003-03-17	00:33:21	49.18	73.30	5.121e-01	1.296e-02	245
2003-03-17	00:42:06	48.42	73.21	5.156e-01	1.454e-02	192
2003-03-18	00:12:28	50.47	73.40	5.041e-01	7.892e-03	459
2003-03-18	00:25:52	49.47	73.33	5.173e-01	9.933e-03	309

Table 2—Continued

Date	Time	Spat. Freq. (1'')	Basel. Angle (° E of N)	V^2	σ_{V^2}	#
2003-03-18	00:33:16	48.85	73.27	5.271e-01	1.035e-02	345
2003-03-21	00:43:22	46.75	72.95	5.772e-01	9.288e-03	385
2003-03-21	00:48:38	46.19	72.85	6.055e-01	2.220e-02	42
2003-03-21	01:06:55	44.07	72.38	6.018e-01	1.650e-02	323
2003-03-22	00:34:15	47.29	73.04	5.797e-01	4.487e-03	454
2003-03-22	00:41:19	46.55	72.92	5.837e-01	4.348e-03	471
2003-03-22	00:48:31	45.77	72.76	5.960e-01	4.632e-03	461
2003-03-27	23:51:52	49.03	73.29	5.253e-01	1.073e-02	460
2003-03-27	23:59:06	48.39	73.21	5.368e-01	1.139e-02	389
2003-03-28	00:06:22	47.71	73.11	5.500e-01	1.248e-02	322
2003-03-28	23:43:31	49.40	73.32	5.304e-01	1.179e-02	400
2003-03-28	23:50:53	48.78	73.26	5.279e-01	1.467e-02	348
2003-03-28	23:58:29	48.09	73.17	5.558e-01	2.190e-02	272
2003-03-29	23:34:06	49.83	73.36	5.201e-01	9.993e-03	447
2003-03-29	23:41:37	49.23	73.31	5.238e-01	1.175e-02	352
2003-03-29	23:49:13	48.58	73.23	5.424e-01	1.325e-02	335
2003-03-30	00:31:28	44.08	72.38	6.009e-01	1.131e-02	459
2003-03-31	23:37:44	48.89	73.27	5.267e-01	2.318e-02	342
2003-04-01	00:03:01	46.45	72.89	5.604e-01	1.989e-02	402

Table 3. VLTI/VINCI observations and derived K -band uniform disk (UD) diameters with associated formal errors.

Date	Mean JD	# of series	Mean Phase	Θ_{UD}^K (mas)	$\sigma(\Theta)$ (mas)	χ_{ν}^2
Jan. 25 - 30	2452666.8	17	0.80	10.52	0.03	0.50
Feb. 04 - 09	2452678.8	10	0.83	10.33	0.07	0.55
Mar. 16 - 21	2452718.0	12	0.92	9.98	0.06	3.91
Mar. 27 - 31	2452728.1	12	0.95	10.16	0.03	0.13

Note. — The observation dates were grouped into 4 bins of 5 days each.

Figure Captions

Fig. 1.— Near-infrared K -band squared visibility amplitudes of S Ori and best fitting uniform disk models for our four VLTI/VINCI epochs.

Fig. 2.— Total intensity image of the $v = 1, J = 1 - 0$ (red) and $v = 2, J = 1 - 0$ (blue) SiO maser emission toward S Ori. The images represent maximum pixel values over the LSR velocity range from $+10.1 \text{ km s}^{-1}$ to $+25.4 \text{ km s}^{-1}$ plotted as contours. Contour levels are 1, 2, 4, 8, 16, 32, 64 times the 3σ off source noise of $0.1 \text{ mJy beam}^{-1}$. Peak flux density is $4.36 \text{ Jy beam}^{-1}$ for the $v = 1, J = 1 - 0$ line and $5.35 \text{ Jy beam}^{-1}$ for the $v = 2, J = 1 - 0$ transition. Synthesized beam sizes are $0.58 \times 0.17 \text{ mas}$ at a position angle of -15.4° for $v = 1, J = 1 - 0$ and $0.52 \times 0.17 \text{ mas}$ at a position angle of -15.7° for $v = 2, J = 1 - 0$.

Fig. 3.— Obtained S Ori K -band uniform disk diameter as a function of date and variability phase. The dashed line denotes the best fitting linear functions to all of our values and to the two closest points to our VLBA epoch. Our VLBA and VLTI variability phases are indicated by arrows.

Fig. 4.— LOS velocity structure of the $v = 1, J = 1 - 0$ SiO maser emission toward S Ori. The top panel shows the spectrum formed by plotting maser intensity versus velocity, color coded in 2 km s^{-1} velocity increments from redward (left) to blueward (right). The solid line in the top panel represents the scalar-averaged cross-power spectrum averaged over all of the VLBA antennas. The bottom panel plots the spatial and velocity distribution of the masers. The color of each point represents the corresponding velocity bin in the spectrum and the size of each point is proportional to the logarithm of the flux density. Errors in the positions of the features are smaller than the data points. The dashed circle is based on the mean angular distance of the SiO masers from the center of the distribution. The colored circle in the center shows the angular size of the photosphere as determined from our VLTI K -band measurements.

Fig. 5.— LOS velocity structure of the $v = 2, J = 1 - 0$ SiO maser emission toward S Ori. The top panel shows the spectrum formed by plotting maser intensity versus velocity, color coded in 2 km s^{-1} velocity increments from redward (left) to blueward (right). The solid line in the top panel represents the scalar-averaged cross-power spectrum averaged over all of the VLBA antennas. The bottom panel plots the spatial and velocity distribution of the masers. The color of each point represents the corresponding velocity bin in the spectrum and the size of each point is proportional to the logarithm of the flux density. Errors in the positions of the features are smaller than the data points. The dashed circle is based on the mean angular distance of the SiO masers from the center of the distribution. The colored circle in the center shows the angular size of the photosphere as determined from our VLTI K -band measurements.

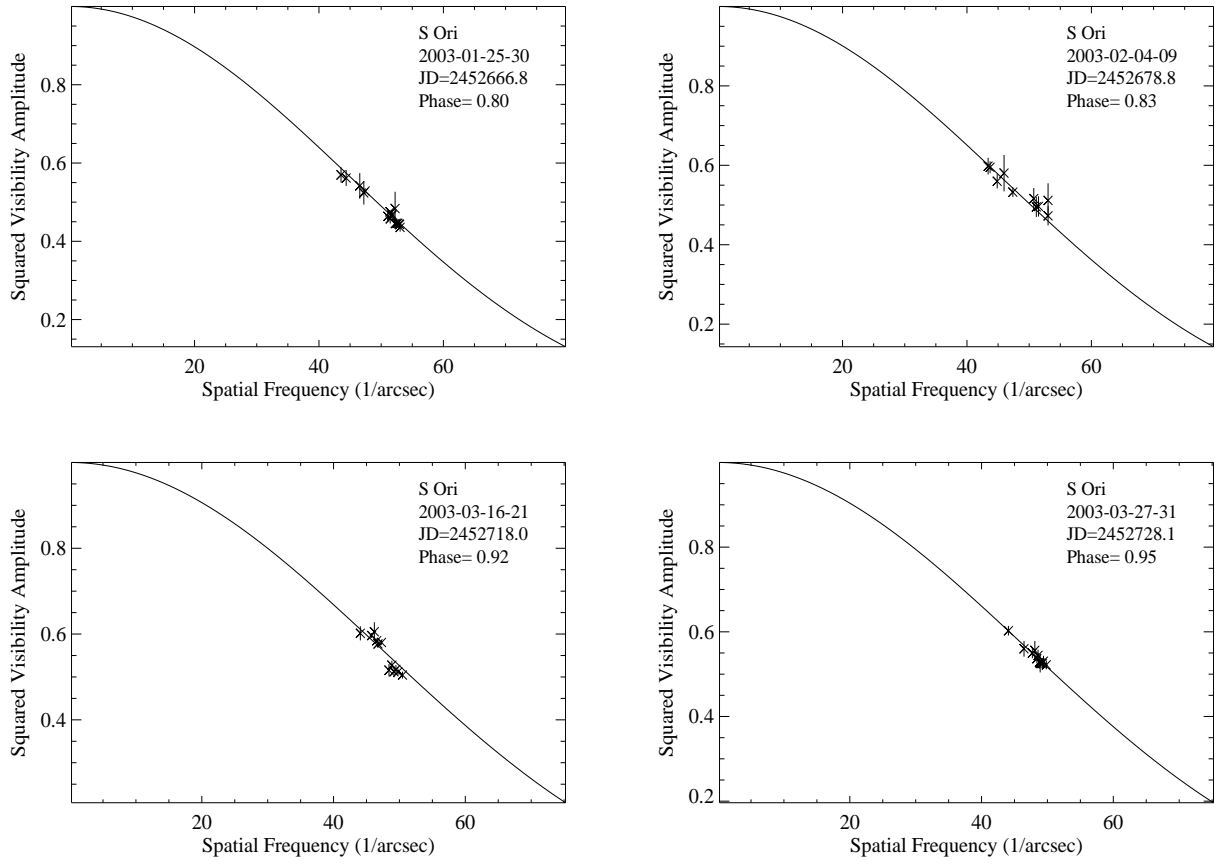


Figure 1

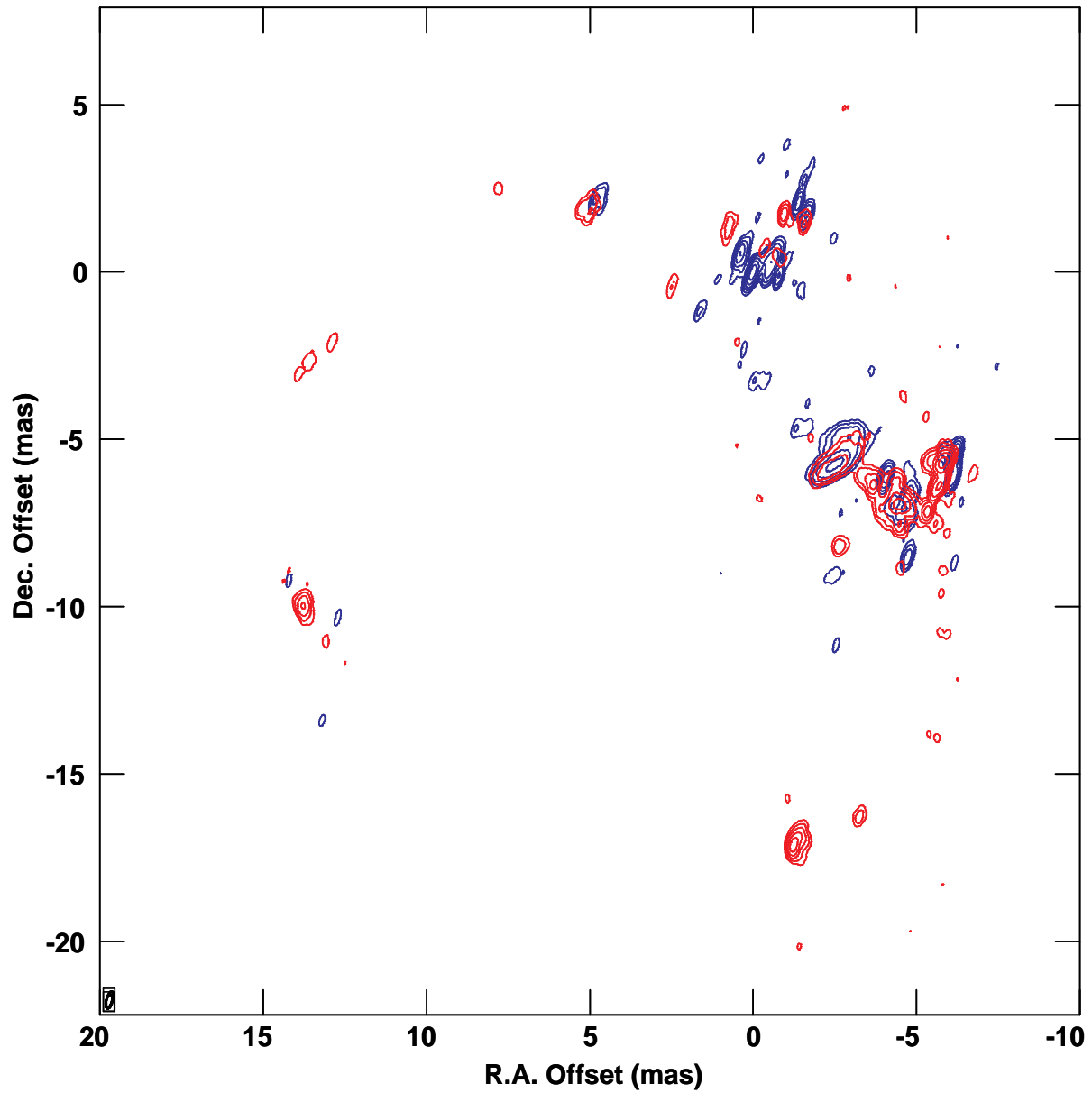


Figure 2

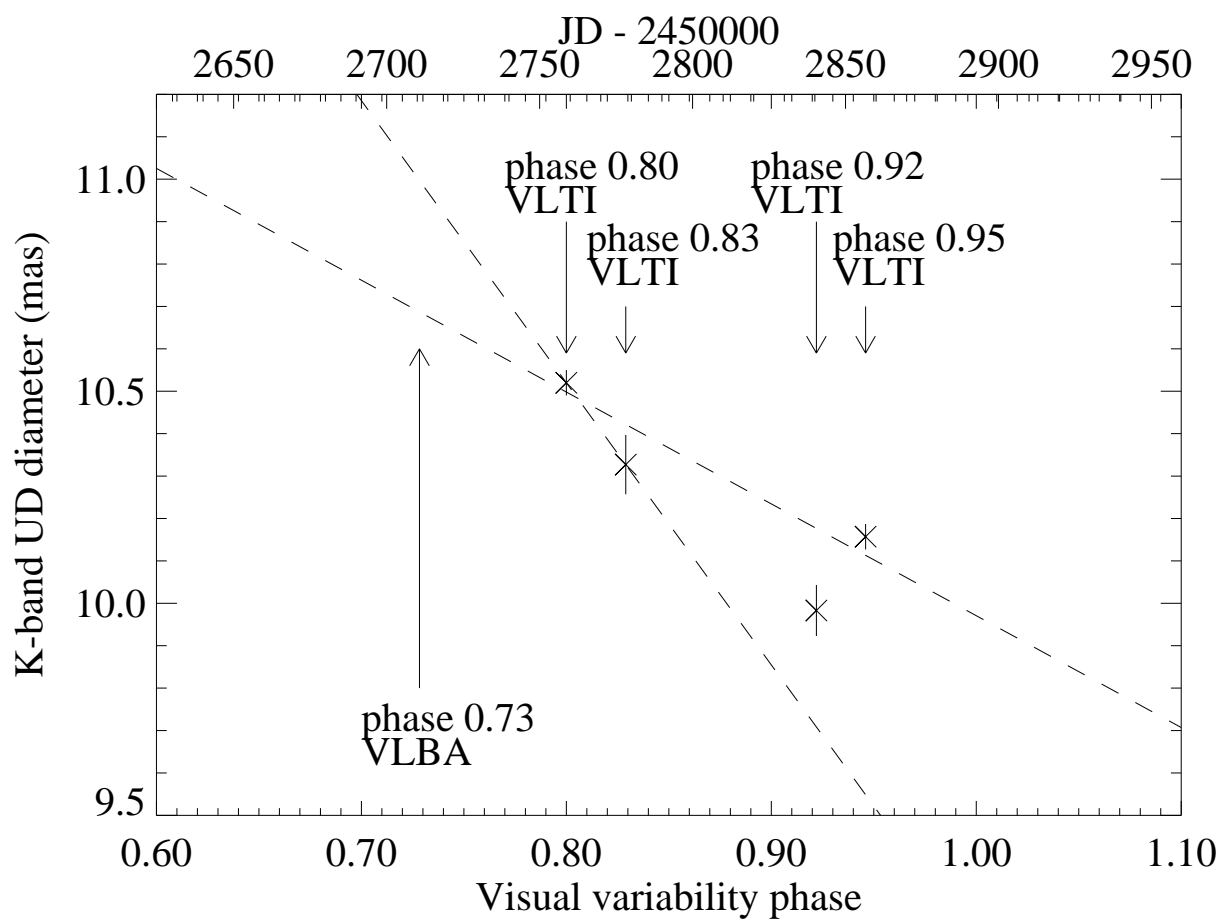


Figure 3

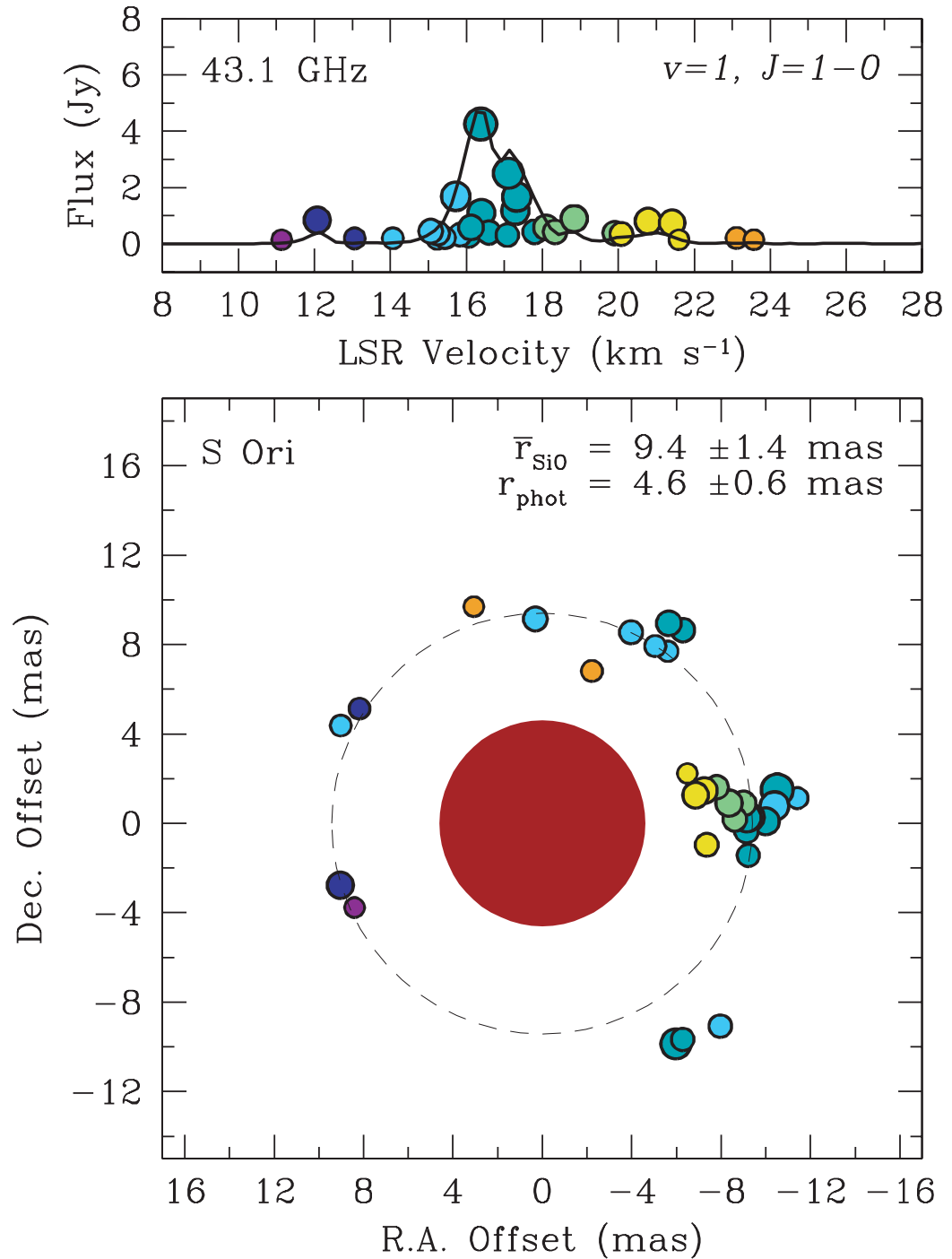


Figure 4

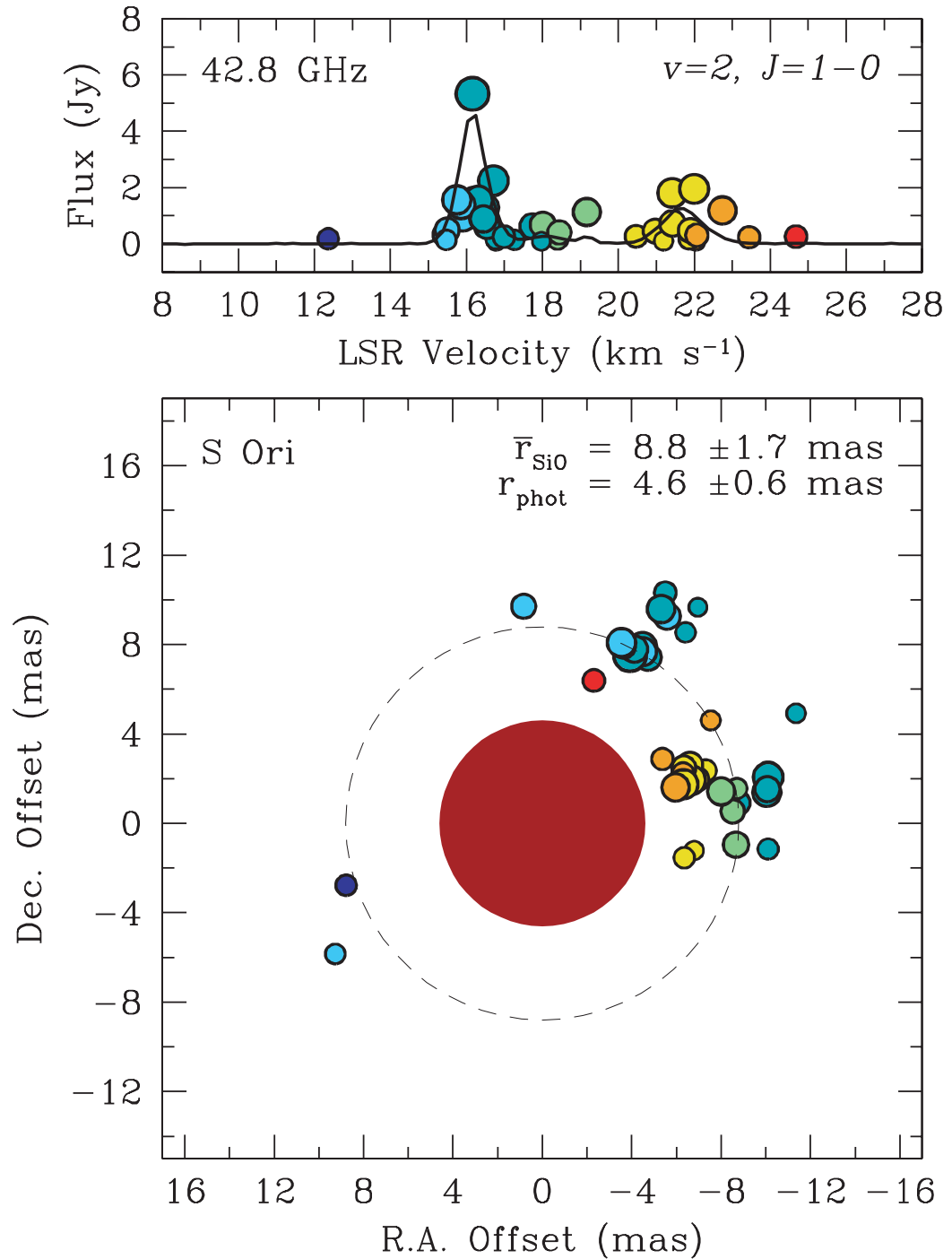


Figure 5